OSR
ORAL SCIENCES REPORTS

Original Article

Received: April 29, 2025
Revised: May 6, 2025
Accepted: June 6, 2025

Corresponding Author:
Weerachai Singhatanadgit,
Department of Oral and Maxillofacial Surgery, Faculty of Dentistry, Thammasat University, Pathum-Thani 12121, Thailand
E-mail: s-wrch@tu.ac.th

Oral Sci Rep. 2025; 46(3): 211-224

Hemolytic Assessment of Geranylgeraniol/ Clindamycin-Loaded Composite Hydrogel

Winita Watcharanon[1], Setthawut Kitpakornsanti[2], Puangwan Lapthanasupkul[3], Boonlom Thavornyutikarn[4], Wanida Janvikul[4], Weerachai Singhatanadgit[1,2]

[1]Department of Oral and Maxillofacial Surgery, Faculty of Dentistry, Thammasat University, Thailand
[2]Research Unit in Mineralized Tissue Reconstruction, Thammasat University, Thailand
[3]Department of Oral and Maxillofacial Pathology, Faculty of Dentistry, Mahidol University, Thailand
[4]National Metal and Materials Technology Center, National Science and Technology Development Agency, Thailand

Abstract

Objectives: This study investigated the hemolytic activity of a geranylgeraniol (GGOH)/ clindamycin (CDM)-loaded composite hydrogel developed as a potential preventive measure for medication-related osteonecrosis of the jaw associated with bisphosphonate (MRONJ-B).

Methods: The surface and structural properties of the drug-loaded hydrogel were characterized using stereomicroscopy, scanning electron microscopy, confocal fluorescence microscopy, and micro-computed tomography. The hemolytic activity of the drug-free (control) and drug-loaded hydrogels was comparatively assessed using three *in vitro* models: washed red blood cells (RBCs), diluted whole blood, and clotted whole blood, to evaluate the impact of the plasma and fibrin matrix on the hemolytic potential of the materials.

Results: The results showed that the drug-loaded hydrogel exhibited an average pore size of 38±24 µm, with a porosity of 84±4.3% and an interconnectivity of 99.9±0.1%. The control hydrogel demonstrated minimal hemolysis (<0.5%) in all test models. While the drug-loaded hydrogel exhibited increased hemolysis (>5%) in both washed RBC and diluted whole blood models, the presence of natural fibrin formation and platelet lysate significantly mitigated the hydrogel's hemolytic activity. Notably, platelet lysate encapsulation provided superior RBC protection compared to natural fibrin within the clotted whole blood model. Histological analysis of the drug-loaded hydrogel in *ex vivo* cultures with clotted whole blood did not reveal significant RBC toxicity.

Conclusions: These findings suggested that the drug-loaded composite hydrogel may be suitable for further *in vivo* investigations of its biocompatibility and efficacy in preventing MRONJ-B.

Keywords: geranylgeraniol, hemolysis, hydrogel, medication-related osteonecrosis of the jaw, platelet lysate

Introduction

Medication-related osteonecrosis of the jaw (MRONJ) associated with bisphosphonates (MRONJ-B) is a condition characterized by necrotic exposed bone in the maxillofacial region that does not heal after 8 weeks in patients who are receiving or have previously received bisphosphonates (BP) and have no history of radiation therapy in the craniofacial region.[1] Recently, dual prolonged releases of geranylgeraniol (GGOH) and clindamycin (CDM) from composite drug carriers, developed for the potential prevention of MRONJ-B, were reported. These composite hydrogels were primarily composed of carboxymethyl chitosan (CMCS) and amine-functionalized mesoporous silica, Mobil Composition of Matter No. 41 (NMCM-41) nanoparticles.[2,3] The biological properties, including *in vitro* and *in vivo* biocompatibility, the ability to reverse the cytotoxicity of zoledronic acid (ZA), and antibacterial activity, of these dual drug-loaded hydrogels have also been reported.[2,3] Several studies have supported the application of GGOH in reversing angiogenesis inhibition[4] and local toxicity[5] of BP. In addition, GGOH may be a potential drug for MRONJ-B prevention due to its ability to maintain a population of viable mesenchymal stem cells (MSCs) with osteogenic efficacy against BP.[6,7] CDM, a widely used antibacterial drug for odontogenic infections, is particularly effective against oral streptococci and strictly anaerobic bacteria[8], and helps control oral bacterial infections, which are identified as an important part of the etiopathogenesis of MRONJ-B.[9] The *in vitro* data suggest that implantation of these GGOH/CDM-releasing NMCM-41/CMCS composite hydrogels into bony extraction sockets may help prevent MRONJ-B in high-risk patients.

Although CMCS exhibits high biocompatibility[10-13], studies have demonstrated that MCM-41 nanoparticles can induce hemolysis exceeding 5% at concentrations ranging from 100 to 500 μg/mL.[14-16] Furthermore, GGOH has been reported to cause significant hemolysis, exceeding 20%, at concentrations above 500 mg/mL.[17] This raised concern about the hemocompatibility of these recently developed GGOH/CDM-releasing NMCM-41/CMCS composite hydrogels, which warrant blood compatibility assessment before the animal and clinical studies

As with intravascular medical devices, hemocompatibility is also important for the local application of blood-contacting extravascular devices, such as implanted biomaterials and the aforementioned GGOH/CDM-releasing NMCM-41/CMCS composite hydrogels. Blood is a complex biological fluid composed of approximately 55% plasma, 44% red blood cells (RBCs), and 1% leukocytes and platelets. To prevent the excessive activation and destruction of blood components, newly developed medical devices must not elicit harmful interactions with blood components, especially RBCs, which are the most abundant blood cells. RBCs are highly susceptible to hemolysis due to shear stress, osmotic pressure fluctuations, and drug-induced oxidative stress.[18] Hemolysis can have a negative impact on tissue healing, resulting in delayed or non-healing tissues.[19] For example, hemolytic RBCs release hemoglobin and heme into surrounding healing tissues. Heme, a damage-associated molecular pattern (DAMP) derived from ruptured RBCs, exerts potent pro-inflammatory and pro-thrombotic effects.[20] It also triggers excessive activation of platelets, endothelial cells, and immune cells and changes the functional properties of plasma proteins.[20] Heme-mediated immune dysregulation may exacerbate infection-associated diseases, such as MRONJ-B. Hemoglobin and heme possess oxidative properties. Specifically, heme has been demonstrated to oxidize low-density lipoprotein, a process that can subsequently trigger the activation of toll-like receptors 2 and 4, leading to the stimulation of pathogenic innate immune cells.[21,22] Moreover, hemolysis also induces the formation of erythrophagocytes, which negatively regulate inflammation and immunity, and may modulate disease-specific outcomes.[19] Damaged RBCs may also impair oxygen delivery to tissues.[23] Since the correlation between *in vitro* hemolysis and *in vivo* toxicity has been reported[24], *in vitro* hemolysis assays are thus crucial for initial biomaterial-blood compatibility assessment, preventing poor tissue healing and potentially severe acute toxic reactions when tested *in vivo*.[25]

To evaluate the potential for *in vivo* biocompatibility and MRONJ prevention of the novel, in-house developed GGOH/CDM-loaded composite hydrogel, it was imperative to first assess its possible hemolytic activity. This study was thus conducted to determine the *in vitro* hemolytic potential of the drug-releasing hydrogel. Furthermore, the influence of biologically relevant factors, such as plasma, fibrin matrix, and platelet lysate (PL) gel encapsulation, on its hemolytic activity was investigated. The study hypotheses were that the drug-loaded hydro-

gel exhibited acceptable hemolytic activity and that the plasma, fibrin matrix and PL gel affected the hemolytic activity of the drug-loaded hydrogel.

Materials and Methods

Materials

Water-soluble CMCS ($\overline{M}_w$=3.0×10^5 Da, degree of substitution (DS)=0.9) and NMCM-41 mesoporous silica nanoparticles were directly prepared in our laboratory, according to the method described in the literature.[2] Clindamycin hydrochloride (MW=479.46 g/mol) and GGOH (MW=290.48 g/mol) were supplied by Sigma-Aldrich Corporation. All analytical-grade chemicals were used as received without further purification.

The Blood Bank at Thammasat University Hospital kindly provided expired leukocyte-poor pooled platelet concentrate (LPPC) and buffy coat samples. Healthy volunteers provided whole blood samples. This study was ethically approved by the Ethics Review Sub-Committee for Research Involving Human Research Subjects of Thammasat University No. 3 (COA No. 068/2564), the Institutional Biosafety Committee of Thammasat University (057/2564).

Preparation of composite hydrogels

A composite hydrogel used in the present study was NMCM-41/CMCS composite hydrogel that was initially fabricated in a disc form with a dimension of 4 mm diameter x 2 mm thickness) and then loaded with 240 mg CDM and 120 µg GGOH per specimen (coded as drug-loaded hydrogel). Both drug-loaded and drug-free (coded as control hydrogel) hydrogels were prepared in our laboratory using the method described in a previous report.[2] All specimens were UV-sterilized for 1 h before being tested.

Preparation of hydrogels encapsulated with human PL gel

The PL was prepared from LPPC containing approximately 1-1.5x10^6 platelets/µL that were subjected to 3 freeze-thaw cycles at 37°C and -80°C. To initiate gelation and form PL gel, 147 µL of PL was mixed with 3 µL of 1 M $CaCl_2$. Subsequently, 30 µL of the mixture was dropped onto each pre-wet hydrogel (4 mm diameter x 2 mm thickness). The PL gel-encapsulated hydrogels were then incubated at 37°C for 45 min to allow complete gelation. The PL gel-encapsulated drug-loaded hydrogel was coded as PL-drug-loaded hydrogel.

Structural characterization of hydrogels and PL gel-encapsulated hydrogels

The pore structure and microstructural morphology of hydrated samples were also examined by using a stereomicroscope, X-ray microcomputer tomography (µCT), confocal fluorescence microscopy, and scanning electron microscopy (SEM). For visual observation under the stereomicroscope, the encapsulated hydrogels were prepared within the PL gel mixed with food-grade purple coloring (Food color violet color, Best odour Co., Ltd). The samples were then visualized under a stereomicroscope (Euromex, Arnhem, The Netherlands).

For the µCT examination, drug-loaded hydrogel and PL-drug-loaded hydrogel specimens were fully hydrated in distilled water overnight and stained with 0.2% Lugol's iodine solution (a mixture of one part iodine and two parts potassium iodide in water) for 24 h and scanned in a container filled with distilled water using a µCT SkyScan 1275 (Bruker µCT, Kontich, Belgium) under the following parameters: pixel size=8 µm, source voltage=40 kV, source current=80 µA, no filter, and rotation step=0.2°. Two- and three-dimensional visualizations of the hydrogel were obtained using DataViewer and CTVox, respectively. Adaptive thresholding and 3D despeckling were employed to segment dense material from voids. Porosity analysis was conducted using CTAn software. Interconnectivity was calculated as the ratio of open pore volume to total pore volume. Total porosity and interconnectivity were determined from analyses of the middle region of the hydrogel specimen.

Autofluorescence of the fibrin matrix within the PL gel was used to visualize the presence of the PL gel in the porous space of the drug-loaded hydrogel specimen. The PL-drug-loaded hydrogel was prepared, and scanning was performed using the Nikon C2plus confocal microscopy (Nikon Corporation, Tokyo, Japan). The specimens were captured using a 20× objective in two channels (green and blue), and the autofluorescence images were then merged. For SEM analysis, samples were exposed to a series of washes with increasing ethanol concentrations of 20%, 50%, 70%, and 100%. The samples were then left to dehydrate completely at 37°C overnight. Finally, the

samples were sputter-coated with gold for 6 min using a sputtering coating machine (Smart Coater, JEOL Ltd., Tokyo, Japan) and subjected to SEM analysis using JEOL NeoScope JCM-6000 scanning electron microscope. (JEOL Ltd., Tokyo, Japan). The average pore sizes were also measured directly from their SEM images using ImageJ with 50 pores per image (n=3).

RBC hemolysis test

In the present study, the hemolysis test was performed using three different models with RBCs and three different blood compositions (Figure 1). These models included (1) washed RBCs, i.e., the tested sample immersed in 1% washed RBCs in phosphate-buffered saline (PBS, pH 7.0), (2) diluted fresh whole blood, i.e., the tested sample immersed in 1% fresh whole blood consisting of similar compositions to the whole blood with 1:100 dilution, and (3) clotted fresh whole blood, i.e., the tested sample encapsulated in a clotted blood with the presence of fibrin matrix. The total volume for each test was maintained at 600 µL for each tested hydrogel.

For washed RBCs and diluted whole blood hemolysis tests, 3 mL of whole blood was collected into a 3-mL VACUETTE Coagulation sodium citrate 3.2% tube. RBC suspensions were prepared by centrifuging freshly drawn blood samples at 1700× g for 5 min. The supernatant was removed and replaced with 2 mL of PBS. This washing procedure was repeated thrice until the supernatant was visually clear. The final RBC pellet was resuspended in PBS to a concentration of 1%. For experiments using diluted fresh whole blood, the washing procedure was omitted, but subsequent experimental steps remained unchanged. In the clotted blood model, fresh whole blood was used without any additional processing steps.

Following 3 h incubation at 37°C of the tested hydrogels with the RBCs, the supernatants were collected by centrifuging at 2000 g for 5 min, and the absorbance at 540 nm was then measured using a microplate spectrophotometer Varioskan® Flash Spectral Scanning Multimode Reader (Thermo Scientific, Waltham, MA, USA). In some experiments, the remaining RBCs were smeared and observed under a light microscope. The mean percentage of spherocytes was quantified across four microscopic fields per group. Meanwhile, the RBCs adhered to the hydrogels were prepared for SEM analysis, as described below. The positive control was prepared by disrupting the RBC membrane with sterile deionized (DI) water, while the negative control consisted of RBCs incubated in PBS. The hemolysis was calculated using the following equation:

$$\text{Hemolysis (\%)} = \frac{OD_{test} - OD_{neg}}{OD_{post} - OD_{neg}} \times 100$$

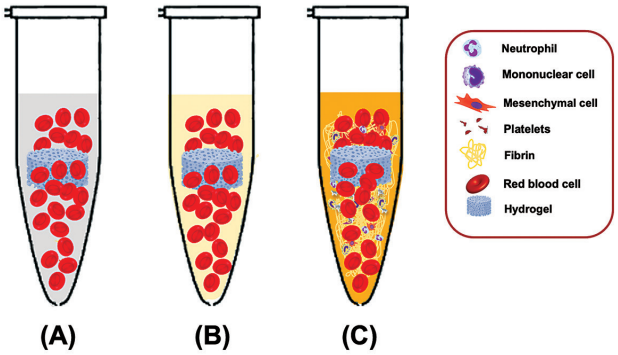

Figure 1: Schematic diagram showing the three different hemolysis models used in the present study. (A), Washed RBCs model consisting of 1% washed RBCs in PBS: (B), Diluted fresh whole blood model containing 1% fresh whole blood, which consisted of 1% RBCs with 5% human plasm in PBS: (C), Clotted fresh whole blood consisting of undiluted RBCs and other blood cells within fibrin network and plasma.

Morphological characteristics of the remaining RBCs on the hydrogel surface

SEM was used to observe morphological features of the remaining RBCs adhering to the hydrogel surface after the hemolysis test. The samples were fixed in 10% formalin for 24 h before dehydration and processing and subsequently examined by SEM, as described above.

Ex vivo cultures of hydrogel-embedded clotted fresh whole blood and histological analysis

Each pre-wet hydrogel was incubated with 600 µL of fresh whole blood in end-cutting inverted 1.5 mL microtubes for 1 h to allow complete blood clotting. Cell culture medium (α-minimum essential medium (Gibco Life Technologies Ltd, Paisley, UK) containing 10% fetal bovine serum supplemented with 200 U/mL penicillin, 200 µg/mL streptomycin, 2 mM L-glutamine (all from Gibco) was added to overflow the microtubes, and incubation continued for an additional 1 h and 24 h in a 37°C incubator with a humidified atmosphere of 5% CO_2. Clotted fresh whole blood samples without hydrogels were also used for comparison. At the end of each time point, the clots

were fixed with 10% formalin for 48 h and transferred to 5% formalin until processed into histological samples. Paraffin sections were cut at a 5-µm thickness, stained with hematoxylin and eosin (H&E), and observed under the Nikon C2plus microscope (Nikon Corporation, Tokyo, Japan) using both brightfield and phase contrast modes. Clotted fresh whole blood samples without hydrogels were used for comparison.

Statistical analyses

Unless otherwise noted, the studies were carried out at least in triplicate, and the results were reported as the mean ± standard deviation (SD) based on three separate experiments. Statistical differences were analyzed using one-way Analysis of Variance (ANOVA) followed by post hoc Bonferroni tests (SPSS software version 26; SPSS, Inc., Chicago, IL). A *p*-value of 0.05 or less was considered statistically significant.

Results and Discussion

Characterization of the hydrogels

The microstructure of the drug-loaded hydrogel is shown in Figure 2. Stereomicroscopic analysis revealed a porous structure and an irregular surface of the drug-loaded hydrogel (Figures 2A and 2B). The fluorescence images obtained from the autofluorescence of CMCS in the blue channel revealed the ultrastructure of non-processed samples, which revealed the porous structure of the drug-loaded hydrogels (Figures 2C and 2D). SEM micrographs in Figures 2E and 2F further demonstrated an interconnected network of pores within the hydrogel, with mesoporous silica nanoparticle agglomerates dispersing throughout the CMCS matrix surface. Measured directly from the SEM images, the average pore size was approximately 38±24 µm. Most pore size fell within a range between 20 µm and 40 µm (Figure 2G). In Figure 2H, the 3D uCT image confirmed the porous structures of the hydrogel with porosity of 84±4.3% and interconnectivity of 99.9±0.1%. The microstructure of the control (drug-free) hydrogel was similar to that of the drug-loaded hydrogel.

Given the interaction between the hydrogel and RBCs, the highly porous structure of the hydrogel, characterized by interconnected pores exceeding 5 µm in diameter, facilitated the diffusion of RBCs throughout its extensive surface area. This intimate contact between RBCs and the hydrogel microstructures positively raises the potential for contact-induced hemolysis, warranting further investigation into the hemolytic activity of the material.

Characterization of PL-encapsulated drug-loaded hydrogels

A previous study has demonstrated that GGOH could induce hemolysis *in vitro*. It is, therefore, plausible that, besides potential contact-induced hemolysis, GGOH released from the drug-loaded hydrogel, as previously reported[3], might contribute to the hemolytic activity of the hydrogel. Our earlier work suggested a role for fibrin gel in the controlled release of GGOH from hydrogels.[2] To mitigate this hemolytic effect, encapsulation within a fibrin-containing PL gel was employed in the present study.

Following the encapsulation of drug-loaded hydrogels within the PL gel mixed with purple food coloring, direct observation under a stereomicroscope showed that the PL-drug-loaded hydrogel surface exhibited reduced porosity and roughness due to the spreading of the purple PL gel into the pores and across the entire surface (Figure 3A). Cross-sectional images of the hydrogels also supported these observations. The PL-drug-loaded hydrogel showed significant penetration of the purple PL gel throughout the material, highlighting the effective infiltration and distribution of the PL gel within the hydrogel (Figure 3A).

A confocal fluorescence microscopy analysis of the PL-drug-loaded hydrogel in Figure 3B demonstrated the formation of PL-derived fibrin within the hydrogel pores. The porous structure of the hydrogel displayed blue autofluorescence in the blue channel, whereas the PL gel containing fibrin exhibited notable green autofluorescence observed in a green channel within the pore structure (Figure 3B). This observation suggested the integration of PL gel coating throughout the surface and internal pores of the hydrogel. In Figure 3C, SEM images reveal pore structure and microstructural morphology of the PL-drug-loaded hydrogel. The PL gel, characterized by a fine mesh-like structure of fibrin fibers, infiltrated into the pores of the hydrogel, as shown in Figure 3C. This suggested that the fibrinous PL gel could fill the material cavities. The formation of the fibrin network of PL gel occurred within

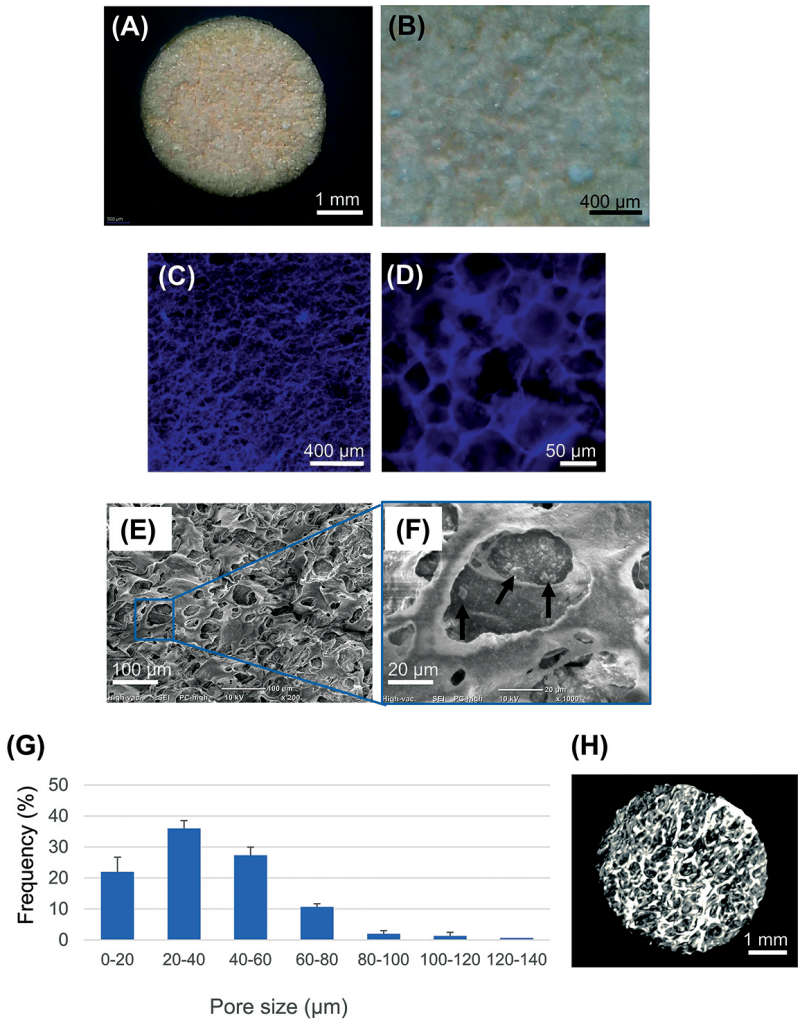

Figure 2: Porous structure of the drug-loaded hydrogel. Surface morphology of the hydrogel under a stereomicroscope at low (A) and high (B) magnifications. Blue channel autofluorescence images at low (C) and high (D) magnifications. Representative SEM images at a low magnification revealing pore interconnectivity (E) and a high magnification showing the agglomeration of mesoporous silica nanoparticles (black arrows) on the hydrogel surface (F). The pore size distribution analysis is shown in (G). The data are presented as mean percent ± SD (n=3). (H) 3D uCT image of the drug-loaded hydrogel.

the porous structure of the hydrogel was consistent with the pore size analysis of the PL-encapsulated drug-loaded hydrogel (Figure 3D), which indicated a reduction in the average pore size compared with that of the non-PL-incapsulated hydrogel. This is likely due to a reduction in the number of smaller pores, resulting in a population of pores with a more uniform size distribution, as shown in Figure 3C. Pore size analysis revealed that both drug-loaded hydrogel and PL-drug-loaded hydrogel had median pore sizes within 20-40 µm (Figure 3D). However, the average pore size of the drug-loaded hydrogel was approximately 62±24 µm, compared with that of 38±24 µm of the PL-drug-loaded hydrogel. An increase in the fibrin-filled pores in the PL-drug-loaded hydrogel was clearly evident by uCT analysis (Figure 3E). The drug-loaded hydrogel encapsulated within PL gel experienced a decrease in total porosity values from 84±4.3% (of the starting drug-loaded hydrogel) to 41±6.9%, while the interconnectivity values before and after encapsulation were 99.9±0.1% and 98±0.3%, respectively. The formation of PL-derived fibrin matrix within the presently studied drug-loaded hydrogel appeared to be similar to that derived from human plasma within the previously reported drug-loaded plasma-treated MCM-41/CMCS composite hydrogel.[2] This would reasonably allow the sufficient diffusion of oxygen/nutrients and the capillary ingrowth to the implanted drug-loaded hydrogel at the tooth extraction site *in vivo*.

In summary, these findings suggested that the

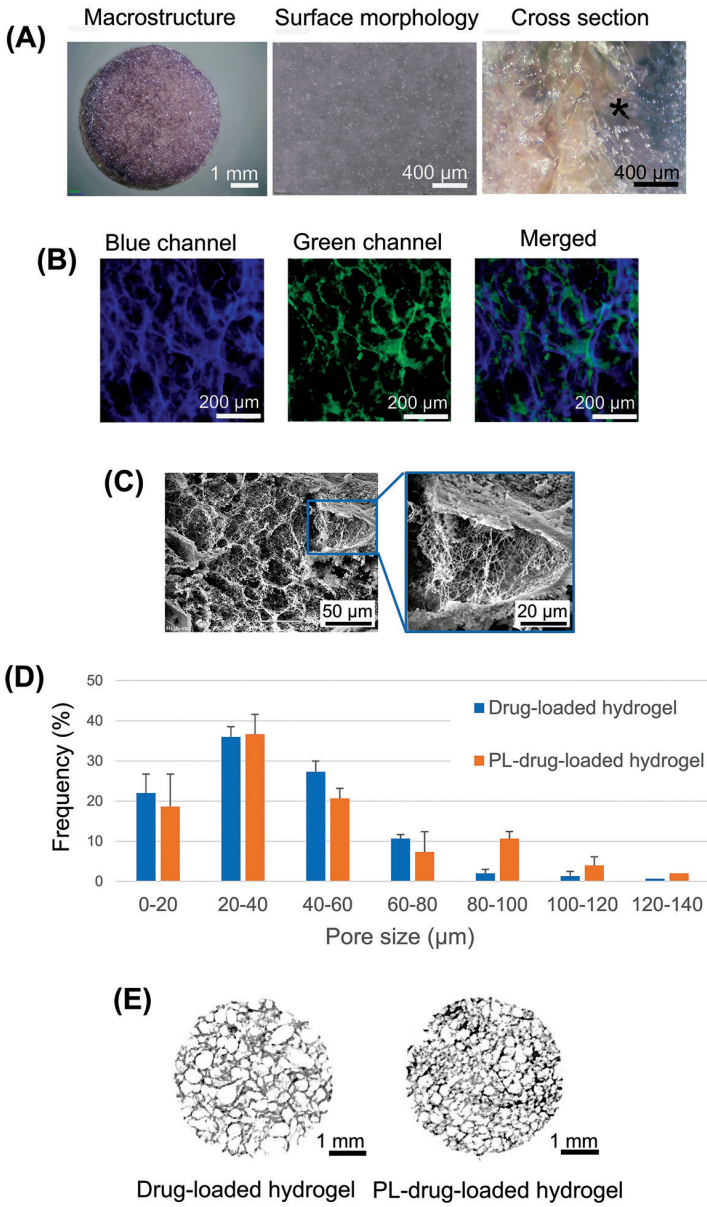

Figure 3: Pore structure and microstructural morphology of PL-drug-loaded hydrogel. (A), Stereomicroscopic images of the PL-drug-loaded hydrogel demonstrated the purple PL gel (*) spreading into the pores, as seen in a cross-sectional aspect: (B), Autofluorescence images of the PL-drug-loaded hydrogel revealed the presence of green autofluorescence of fibrin within the PL gel and blue autofluorescence of the hydrogel porous structure: (C), SEM images revealed the pore structure and microstructural morphology of the PL-drug-loaded hydrogel: (D), A summary of pore size distribution analysis comparing PL-drug-loaded hydrogel with drug-loaded hydrogel. The data are presented as a mean percent±SD (n=3): (E), 2D uCT images of the drug-loaded and PL-drug-loaded hydrogels.

encapsulation of the PL gel allowed it to penetrate into the pore structure of the drug-loaded hydrogel. This might act as a barrier to protect RBCs from direct contact with the hydrogel surface, thus potentially preventing RBC lysis.

Assessment of hemolytic activity of drug-loaded hydrogels in three different *ex vivo* models

To evaluate the hemolysis of the control (drug-free), drug-loaded, and PL-drug-loaded hydrogels, three different models, i.e., washed RBCs, diluted fresh whole blood, and clotted fresh whole blood, were used. As shown in Figure 4A, the hemolysis rate of the control hydrogel exhibited minimal values in washed RBCs, diluted fresh whole blood, and clotted fresh whole blood, measuring 0.27±0.32%, 0.11±0.19%, and 0.35±0.002%, respectively. These were much below the 2% threshold considered for

non-hemolytic materials in all three models tested[26], indicating the excellent compatibility of the control hydrogel with RBCs. In contrast, the drug-loaded hydrogel demonstrated significantly increased hemolysis rates compared with the control hydrogel in the models using washed RBCs and diluted fresh whole blood, measuring 5.45±1.63% and 8.43±4.72%, respectively. These values exceed the acceptable limit of 5% hemolysis[26], suggesting potential RBC toxicity of the drug-loaded hydrogel. Interestingly, the hemolysis of the drug-loaded hydrogel in clotted fresh whole blood was significantly lower at 3.98±1.04%, compared with the diluted fresh whole blood model (8.43±4.72%). After encapsulation with PL, the PL-drug-loaded hydrogel demonstrated significantly reduced hemolysis rates compared with the drug-loaded hydrogel in all three models, measuring 1.41±0.16%, 3.13±0.30%, and 1.93±0.53%, respectively, well below the acceptable limit of 5% for hemocompatible materials. Moreover, the study found that the hemolysis of the PL-drug-loaded hydrogel was significantly different across the three models, with the highest rate observed in diluted fresh whole blood and the lowest in clotted fresh whole blood.

The corresponding hemolysis images of RBCs in a diluted fresh whole blood model are displayed in Figure 4B. The transparency of the supernatant in the control hydrogel was similar to that of the baseline hemolysis in the negative control group (PBS), whereas the red-color supernatant of the positive control, prepared using DI water indicated complete RBC lysis. Figure 4C shows the hemolysis images of RBCs in the clotted fresh whole blood model. Notably, both drug-loaded and PL-drug-loaded hydrogels exhibited red discoloration in the supernatant, which was lighter than that of the positive control, indicating partial RBC lysis.

The morphology of the remaining RBCs after the hemolysis test was also investigated using a phase-contrast microscope and SEM, and the results are shown in Figures 4D and 4E, respectively. In the drug-loaded hydrogel group, non-adherent RBCs exhibited a spherical morphology, characteristic of spherocytes (black arrows). No spherocytes were observed in the control group. However, quantitative analysis revealed that the drug-loaded hydrogel significantly increased the spherocyte percentage to 17%. Conversely, in the PL-drug-loaded hydrogel group, this percentage was markedly reduced to approximately 0.8%, comparable to that in the control group. Additionally, RBCs with a "shooting target" appearance, characterized by a dark center surrounded by a white ring and a dark outer peripheral rim, consistent with target cells (green arrows), were also observed. Blue arrows indicate hollow RBC membrane remnants devoid of cytoplasmic content. SEM analysis revealed that RBCs exhibited a spherical morphology on the surface of the drug-loaded hydrogel, in contrast to the normal biconcave disc-shaped RBCs observed on the control hydrogel surface (Figure 4E). Notably, RBCs treated with the PL-drug-loaded hydrogel primarily displayed a normal biconcave morphology, although some macrocytes were observed, and the incidence of altered RBC shapes was significantly reduced (Figure 4D). These findings supported the hemolysis-protective ability of PL encapsulation for the drug-loaded hydrogel.

It is important to note that a small number of RBCs observed in all groups, including the control PBS group, exhibited echinocytic characteristics, characterized by uniformly distributed, short projections extending from their surface (yellow arrows). Echinocytosis is often considered an *in vitro* artifact, potentially arising from sample preparation or storage conditions.[27] Alterations in RBC plasma membrane integrity can increase membrane permeability, leading to cell swelling, spherocytosis, and ultimately, hemolysis.[28,29] Therefore, spherocytic morphology may be one of the key characteristics of hemolysis.[30]

The control hydrogel, primarily composed of CMCS, previously considered a non-hemolytic material[31-33], exhibited minimal hemolysis, far below the 2% threshold, eliciting hemolysis about 1-1.5%. Unlike the control hydrogel, the drug-loaded hydrogel released significant levels of CDM and GGOH during the first 24 h[3], which likely caused high hemolysis activity of the drug-loaded hydrogel. Exposure to CDM (up to 100 μg/mL) for 3 h caused very low hemolysis of less than 0.1% (data not shown). During the first 24 h, the cumulative release of CDM of the present drug-loaded hydrogel was approximately 149 μg/mL.[3] This released CDM amount was unlikely to cause hemolysis of the drug-loaded hydrogel tested. Moreover, CDM is also not known to cause hemolysis *in vivo*.[34] In contrast to CDM, GGOH presented evidence of hemolysis. GGOH at an extremely high concentration of 1.725 mM showed a significantly high hemolysis percentage of 26.4%.[17] Moreover, GGOH

at 100 μM induced 1% hemolysis and co-treatment with CDM at 100 μg/mL did not further induce hemolysis (data not shown). Within the cells, GGOH is converted into geranylgeranyl pyrophosphate (GGPP), which, in turn, activates the enzyme GGTase-I, which plays a role in the geranylgeranylation of Rac1. Activated Rac1 stimulates NADPH oxidase and subsequently generates reactive oxygen species (ROS).[35] The increased ROS production leads to oxidative stress, damaging the cell membrane and causing cell dysfunction and stiffness, ultimately contributing to increased hemolysis.[36] It is thus likely that the high hemolysis activity of the drug-loaded hydrogel is a result of the burst release of GGOH, particularly at the material surface.

The finding that the hemolysis of the PL-drug-loaded hydrogel differed significantly across the three models suggested the involvement of PL-derived fibrin matrix and plasma mediators in GGOH-induced hemolysis of the drug-loaded hydrogel. Fibrin formation within GGOH-loaded hydrogels has been reported to decrease GGOH release by reducing the exposed hydrogel surface area and interacting with released GGOH molecules.[2] Given that GGOH-induced hemolysis might induce oxidative stress in RBCs, human plasma might contribute to anti-hemolysis through plasma oxidation-counteracting molecules. These include α1-Microglobulin (A1M) and albumin, which bind to heme and neutralize ROS[37,38], thereby protecting against oxidative damage and reducing hemolysis. Moreover, in clotted fresh whole blood, the hemolysis of the PL-drug-loaded hydrogel was significantly lower than that of the drug-loaded hydrogel, indicating that encapsulating the drug-loaded hydrogel with PL gel provided superior protection against hemolysis compared with plasma-derived fibrin spontaneously formed in the clotted fresh whole blood. The presence of certain biomolecules in PL might help prevent hemolysis. Insulin-like growth factor (IGF-1) present in PL increases the activity of glutathione peroxidase (GPX), a crucial antioxidant enzyme.[39] PL also contains antioxidant biomolecules, including superoxide dismutase, glutathione peroxidase, and catalase.[40] Whether PL-mediated reduction of GGOH-induced hemolysis of drug-loaded hydrogels has clinical significance warrants further investigation.

According to International organization for standardization (ISO) standards, devices that have direct contact with circulating blood should undergo hemolysis testing.[26] Similarly, American society for testing and materials (ASTM) standards recommend a 5% hemolysis threshold as the acceptable limit for blood-contacting biomaterials.[41] This 5% limit specifically applies to direct contact with circulating blood devices such as endovascular grafts or pacemaker leads, which can potentially cause systemic hemolysis. In contrast, hydrogels are classified as extravascular implant devices that primarily interact with tissue rather than blood. As a result, they may cause localized hemolysis, for which no specific hemolysis threshold has been established. Assuming a normal hemoglobin concentration of 15 g/dL (or 150 mg/mL), a 1% hemolysis would release approximately 1.5 mg/mL of hemoglobin. Hemoglobin at 2 mg/mL can induce pro-inflammatory cytokine expression in macrophages[42], while hemoglobin at 1 mg/mL also significantly disrupts mitochondrial function and microvascular endothelial barriers.[43] This can lead to increased macrophage apoptosis, chronic inflammation, tissue damage, and delayed wound healing.[19] These *in vitro* studies suggested that 1% hemolysis might potentially have detrimental effects on wound healing. The clinical significance of 1% hemolysis on wound healing remains unclear. *In vivo* data are essential to establish the safe hemolysis threshold for extravascular medical devices.

To evaluate the potential hemolytic effects of the drug-loaded hydrogel intended for placement in extraction sockets, a three-dimensional whole blood clot model was employed. This approach offers several advantages, including its physiological relevance and its capacity to capture the intricate interactions within the clot. By accurately replicating the complex three-dimensional structure and physiological conditions of a blood clot, this model enables the assessment of hemolytic potential within a more realistic environment, encompassing the interactions between blood cells, platelets, and the fibrin network. Due to the absence of a standardized protocol for analyzing hemolysis in whole blood clots, a previously published protocol was adapted to suit its specific needs.[44,45] This three-dimensional clotted whole blood model mimics *in vivo* conditions for local tissue implantation and may, therefore, be beneficial for hemolysis assessment of extravascular medical devices.

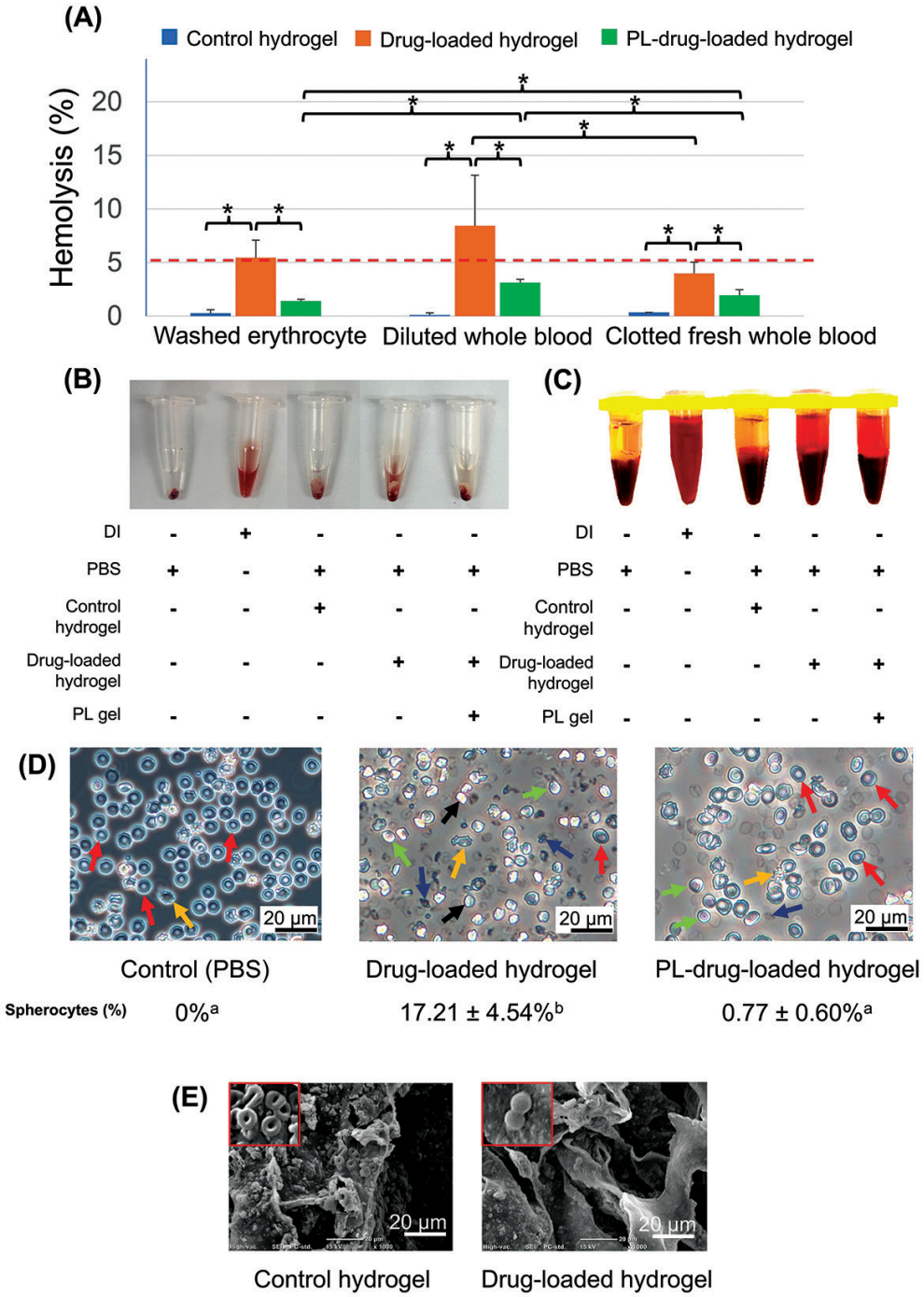

Figure 4: Hemolysis test of the control (drug-free), drug-loaded, and PL-drug-loaded hydrogels. Three different hemolysis models, using washed RBCs, diluted fresh whole blood, and clotted fresh whole blood, were conducted as described in the Materials and Methods. (A) Hemolysis percentages were determined for control, drug-loaded, and PL-drug-releasing hydrogels in washed RBCs, diluted fresh whole blood, and clotted fresh whole blood models. Data are presented as mean percentage±SD (n=6), with *p<0.05 indicating statistical significance. Visual inspection was performed on microcentrifuge tubes containing diluted fresh whole blood (B) and clotted fresh whole blood (C) samples. These samples were exposed to composite hydrogel, DI water (positive control), and PBS (negative control). The presence of red discoloration in the supernatant, indicating RBCs lysis. (D) RBC morphology of blood smears, which were prepared from the remaining RBCs in the diluted fresh whole blood model examined under a light microscope. Various RBC morphologies were observed, including normal biconcave RBCs (red arrows), spherocytes (black arrows), target cells (green arrows), ghost cell (blue arrows), and echinocytes (yellow arrows). Spherocyte percentages are reported as mean±SD (n=4). Distinct uppercase letters denote statistically significant differences among mean spherocyte percentages (p<0.05). (E) SEM imaging of adherent RBC morphology to the drug-loaded and PL-drug-loaded hydrogels in the diluted fresh whole blood model.

Histological analysis of *ex vivo* culture of clotted fresh whole blood with drug-loaded hydrogel

After 1 h incubation of *ex vivo* cultures of clotted fresh whole blood individually with control and drug-loaded hydrogels, H&E staining revealed three distinct zones in both groups (Figure 5). The material zone exhibited a porous structure with interconnected channels, facilitating the penetration of blood components. An edematous zone was observed, characterized by loose tissue containing fibrin fibers and scattered inflammatory cell infiltrates. Finally, a hemorrhagic zone included collections of RBCs which were observed at the peripheral areas of the fibrin layer. Some RBCs were also seen within the peripheral pores of the hydrogel (arrow heads) and forming clusters or aggregates at the material periphery (arrows). These three zones were still observed at 24 h of incubation, although a decrease in the edematous zone was noted. H&E images of clotted whole blood cultured without hydrogel served as controls, demonstrating the characteristic features of the *ex vivo* culture.

Figure 6 demonstrates the high magnification of H&E images of the *ex vivo* cultures, highlighting RBCs morphology and fibrin network within a pore-structured hydrogel. The results showed that normal RBCs shape and size as well as the fibrin matrix containing potentially activated platelets were observed in both hydrogels, comparable to those seen in the control clotted blood (no hydrogel group). Additionally, fibrin fibers were also able to adhere to the surface of both hydrogels and fully fill the pore spaces. These findings suggested that in *ex vivo* clotted blood culture, the drug-loaded hydrogel appeared hemocompatible, compared to both control hydrogel and clotted blood. The fibrin layer adhering to the scaffold surface likely reduced burst drug release and prevented direct contact between RBCs and the hydrogel pore surface, mechanisms that may inhibit toxicity to RBCs. As a result, the RBCs remained intact and retained their normal morphology, as shown in Figure 6. This was consistent with the hemolysis results, which showed that the clotted fresh whole blood model had a lower hemolysis percentage for the drug-loaded hydrogel than both washed RBCs and diluted fresh whole blood models.

The present study has some limitations that should be acknowledged. The 3-h hemolysis incubation, while standard, may not fully capture the long-term, dose-time-dependent hemolytic activity of released GGOH observed in previous studies. Furthermore, the focus on RBC interactions may overlook potential critical effects on other vital cell types, such as platelets and immune cells. Finally, the inherent variability in PL composition introduces a challenge for reproducibility in clinical applications.

Conclusions

The recently developed GGOH/CDM-releasing NMCM-41/CMCS composite hydrogel elicited varying degrees of hemolysis in three distinct experimental models (i.e., 5.45±1.63%, 8.43±4.72%, and 3.98±1.04% in models utilizing washed RBCs, diluted fresh whole blood, and clotted whole blood, respectively). The control, drug-free hydrogel, exhibited excellent compatibility with RBCs across all models, inducing hemolysis of less than 0.5%. Compared with the washed RBC model, an elevation in plasma proteins within the diluted fresh whole blood model exacerbated the hemolytic response of the dual drug-loaded hydrogel, potentially attributable to an augmented release of protein-bound GGOH into the surrounding environment. Conversely, the presence of a fibrin matrix within the PL encapsulation and within the *ex vivo* clotted whole blood model contributed to a diminished release of GGOH from the hydrogel and mitigated direct contact between RBCs and the hydrogel surface, thereby attenuating hemolysis. While encapsulating the hydrogel within a PL gel significantly suppressed hemolysis, providing superior RBC protection compared to that afforded by natural fibrin in clotted whole blood, histological analysis of the drug-loaded hydrogel revealed no significant toxicity to RBCs within the clotted whole blood culture. The present findings suggested that the dual drug-loaded composite hydrogel fulfilled the safety criteria prior to *in vivo* investigations of biocompatibility and preventive efficacy for MRONJ-B.

Acknowledgments

The present study was supported by the Faculty of Dentistry, Thammasat University Research Fund (Contract No. 8/2566) and the Thammasat University Research Unit in Mineralized Tissue Reconstruction, Thailand. The authors also thank the Blood Bank at Thammasat University Hospital for kindly providing expired LPPC and buffy coat samples.

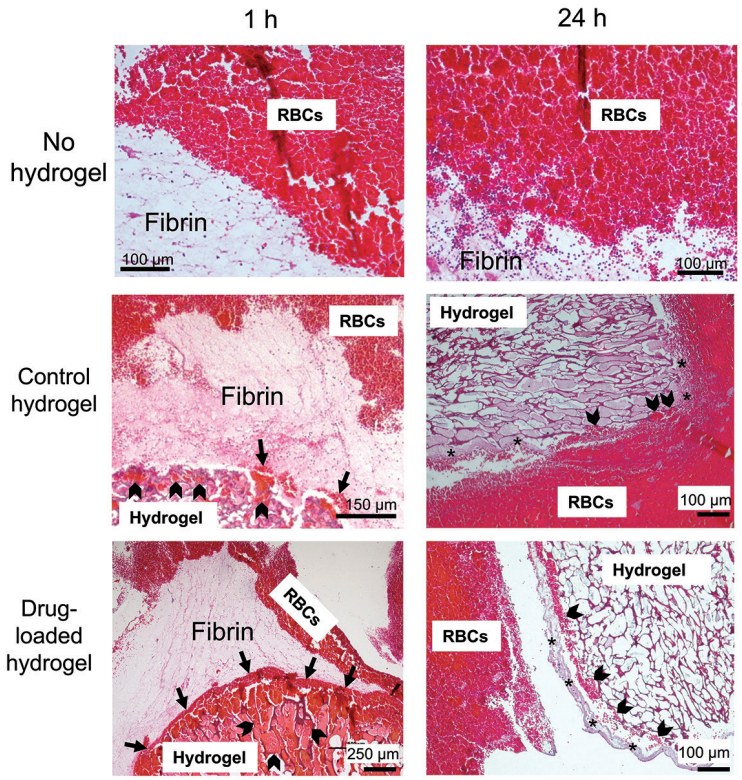

Figure 5: H&E staining of 1-h and 24-h *ex vivo* cultures of clotted human whole blood individually with control and drug-loaded hydrogels revealed the following three zones: The Material zone was composed of the hydrogel. The edematous zone was a loose area surrounding the material, containing scattered inflammatory cells and fibrin (marked as black asterisks). The hemorrhagic zone consisted of collections of RBCs, indicating hemorrhage, and was observed at the periphery of the sections. RBCs were also observed within the peripheral pores of the hydrogel (arrowheads) and formed clusters or aggregates at the material's periphery (arrows).

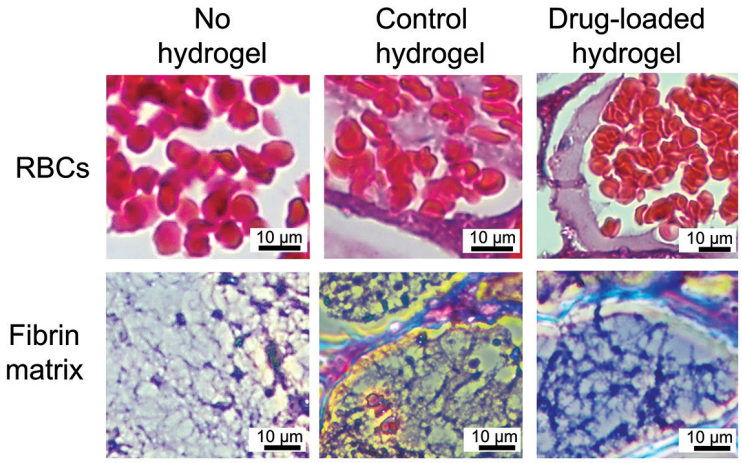

Figure 6: Representative H&E histological images showed RBCs visualized under light microscopy, along with platelets and fibrin fibers visualized under phase-contrast microscopy within the hydrogel, appearing as purple or blue structures. These images were obtained after 24 h of *ex vivo* cultures of clotted human whole blood, either with control or drug-loaded hydrogels. The clotted whole blood culture with no hydrogel, was used as a control.

References

1. Ruggiero SL, Dodson TB, Aghaloo T, Carlson ER, Ward BB, Kademani D. American association of oral and maxillofacial surgeons' position paper on medication-related osteonecrosis of the jaws-2022 update. J Oral Maxillofac Surg. 2022;80(5):920-43.
2. Sungkhaphan P, Thavornyutikarn B, Muangsanit P, Kaewkong P, Kitpakornsanti S, Pornsuwan S, *et al*. Dual-functional drug delivery system for bisphosphonate-related osteonecrosis prevention and its bioinspired releasing model and *in vitro* assessment. ACS Omega. 2023;8(29):26561-76.
3. Thavornyutikarn B, Sungkhaphan P, Kaewkong P, Pornsuwan S, Risangud N, Singhatanadgit W, *et al*. Biodegradable dual-function nanocomposite hydrogels for prevention of bisphosphonate-related osteonecrosis of the jaw. ACS Appl Bio Mater. 2023;6(4):1658-75.
4. Ziebart T, Pabst A, Klein MO, Kämmerer P, Gauss L, Brüllmann D, *et al*. Bisphosphonates: restrictions for vasculogenesis and angiogenesis: inhibition of cell function of endothelial progenitor cells and mature endothelial cells *in vitro*. Clini Oral Investig. 2011;15:105-11.
5. Pabst A, Krüger M, Sagheb K, Ziebart T, Jacobs C, Blatt S, *et al*. The influence of geranylgeraniol on microvessel sprouting after bisphosphonate substitution in an *in vitro* 3D-angiogenesis assay. Clini Oral Investig. 2017;21:771-8.
6. Singhatanadgit W, Hankamolsiri W, Janvikul W. Geranylgeraniol prevents zoledronic acid-mediated reduction of viable mesenchymal stem cells via induction of Rho-dependent YAP activation. R Soc Open Sci. 2021;8(6):202066.
7. Sungkhaphan P, Thavornyutikarn B, Kaewkong P, Pongkittiphan V, Pornsuwan S, Singhatanadgit W, *et al*. Antibacterial and osteogenic activities of clindamycin-releasing mesoporous silica/carboxymethyl chitosan composite hydrogels. R Soc Open Sci. 2021;8(9):210808.
8. Chow M, douglas, and bennett's. Infections of the oral cavity, neck, and head. Mandell, douglas, and bennett's principles and practice of infectious diseases: Elsevier; 2015. p. 789-805. e2.
9. Shibahara T. Antiresorptive agent-related osteonecrosis of the jaw (ARONJ): a twist of fate in the bone. Tohoku J Exp Med. 2019;247(2):75-86.
10. Fan L, Yi J, Tong J, Zhou X, Ge H, Zou S, *et al*. Preparation and characterization of oxidized konjac glucomannan/carboxymethyl chitosan/graphene oxide hydrogel. Int J Biol Macromol. 2016;91:358-67.
11. Wahid F, Yin JJ, Xue DD, Xue H, Lu YS, Zhong C, *et al*. Synthesis and characterization of antibacterial carboxymethyl Chitosan/ZnO nanocomposite hydrogels. Int J Biol Macromol. 2016;88:273-9.
12. Chen L, Du Y, Tian Z, Sun L. Effect of the degree of deacetylation and the substitution of carboxymethyl chitosan on its aggregation behavior. J Polym Sci Part B: Polym Phys 2005;43(3):296-305.
13. Zhang L, Guo J, Zhou J, Yang G, Du Y. Blend membranes from carboxymethylated chitosan/alginate in aqueous solution. J Appl Polym Sci. 2000;77(3):610-6.
14. Yu T, Malugin A, Ghandehari H. Impact of silica nanoparticle design on cellular toxicity and hemolytic activity. ACS Nano. 2011;5(7):5717-28.
15. Davidson S, Lamprou DA, Urquhart AJ, Grant MH, Patwardhan SV. Bioinspired silica offers a novel, green, and biocompatible alternative to traditional drug delivery systems. ACS Biomate Sci Eng. 2016;2(9):1493-503.
16. Joglekar M, Roggers RA, Zhao Y, Trewyn BG. Interaction effects of mesoporous silica nanoparticles with different morphologies on human red blood cells. Rsc Adv. 2013;3(7):2454-61.
17. Lopes MV, Desoti VC, Caleare AdO, Ueda-Nakamura T, Silva SO, Nakamura CV. Mitochondria superoxide anion production contributes to geranylgeraniol-induced death in leishmania amazonensis. Evid Based Complement Alternat Med. 2012;2012(1):298320.
18. Weber M, Steinle H, Golombek S, Hann L, Schlensak C, Wendel HP, *et al*. Blood-contacting biomaterials: *in vitro* evaluation of the hemocompatibility. Front Bioeng Biotechnol. 2018;6:99.
19. Humar R, Schaer DJ, Vallelian F. Erythrophagocytes in hemolytic anemia, wound healing, and cancer. Trends Mol Med. 2022;28(11):906-15.
20. Dimitrov JD, Roumenina LT, Perrella G, Rayes J. Basic mechanisms of hemolysis-associated thrombo-inflammation and immune dysregulation. Arterioscler Thromb Vasc Biol. 2023;43(8):1349-61.
21. Bekkering S, Quintin J, Joosten LA, van der Meer JW, Netea MG, Riksen NP. Oxidized low-density lipoprotein induces long-term proinflammatory cytokine production and foam cell formation via epigenetic reprogramming of monocytes. Arterioscler Thromb Vasc Biol. 2014;34(8):1731-8.
22. Manček-Keber M, Frank-Bertoncelj M, Hafner-Bratkovič I, Smole A, Zorko M, Pirher N, *et al*. Toll-like receptor 4 senses oxidative stress mediated by the oxidation of phospholipids in extracellular vesicles. Sci Signal. 2015;8(381):ra60.
23. Qian Q, Nath KA, Wu Y, Daoud TM, Sethi S. Hemolysis and acute kidney failure. Am J Kidney Dis. 2010;56(4):780-4.
24. Lu S, Duffin R, Poland C, Daly P, Murphy F, Drost E, *et al*. Efficacy of simple short-term *in vitro* assays for predicting the potential of metal oxide nanoparticles to cause pulmonary inflammation. Environ Health Perspect. 2009;117(2):241-7.
25. Dobrovolskaia MA, McNeil SE. Understanding the correlation between *in vitro* and *in vivo* immunotoxicity tests for nanomedicines. J Control Release. 2013;172(2):456-66.
26. ISO. ISO 10993-4: biological evaluation of medical devices part 4—selection of tests for interactions with blood. International Organization for Standardization: Geneva,

Switzerland. 2017.
27. Dalal BI, Brigden ML. Artifacts that may be present on a blood film. Clin Lab Med. 2002;22(1):81-100.
28. Baldwin JM, Lucy JA. Chemically induced fusion of erythrocyte membranes. Methods in enzymology. 220: Elsevier; 1993. p.161-73.
29. Ahkong Q, Fisher D, Tampion W, Lucy J. The fusion of erythrocytes by fatty acids, esters, retinol and α-tocopherol. Biochem J. 1973;136(1):147-55.
30. Behling-Kelly E. Identifying erythrocyte injury in toxicology studies. Toxicol Pathol. 2022;50(7):883-5.
31. Li X, Kong X, Zhang Z, Nan K, Li L, Wang X, *et al*. Cytotoxicity and biocompatibility evaluation of N, O-carboxymethyl chitosan/oxidized alginate hydrogel for drug delivery application. Int J Biol Macromol. 2012;50(5):1299-305.
32. Fu D, Han B, Dong W, Yang Z, Lv Y, Liu W. Effects of carboxymethyl chitosan on the blood system of rats. Biochem Biophys Res Commun. 2011;408(1):110-4.
33. Liu L, Lv Q, Zhang Q, Zhu H, Liu W, Deng G, *et al*. Preparation of carboxymethyl chitosan microspheres and their application in hemostasis. Disaster Med Public Health Prep. 2017;11(6):660-7.
34. Gray JE, Weaver RN, Moran J, Feenstra ES. The parenteral toxicity of clindamycin 2-phosphate in laboratory animals. Toxicol Appl Pharmacol. 1974;27(2):308-21.
35. Chen GP, Yang J, Qian GF, Xu WW, Zhang XQ. Geranylgeranyl transferase-i knockout inhibits oxidative injury of vascular smooth muscle cells and attenuates diabetes-accelerated atherosclerosis. J Diabetes Res. 2020;2020(1): 7574245.
36. Orrico F, Laurance S, Lopez AC, Lefevre SD, Thomson L, Möller MN, *et al*. Oxidative stress in healthy and pathological red blood cells. Biomolecules. 2023;13(8):1262.
37. Kristiansson A, Gram M, Flygare J, Hansson SR, Åkerström B, Storry JR. The role of α1-microglobulin (A1M) in erythropoiesis and erythrocyte homeostasis—therapeutic opportunities in hemolytic conditions. Int J Mol Sci. 2020;21(19):7234.
38. Taverna M, Marie AL, Mira JP, Guidet B. Specific antioxidant properties of human serum albumin. Ann Intensive Care. 2013;3(1):4.
39. Higashi Y, Pandey A, Goodwin B, Delafontaine P. Insulin-like growth factor-1 regulates glutathione peroxidase expression and activity in vascular endothelial cells: Implications for atheroprotective actions of insulin-like growth factor-1. Biochim Biophys Acta. 2013;1832(3):391-9.
40. Yoon JY, Vu HT, Lee JH, Shin JS, Kim HW, Lee HH, *et al*. evaluation of human platelet lysate as an alternative to fetal bovine serum for potential clinical applications of stem cells from human exfoliated deciduous teeth. Cells. 2024;13(10):847.
41. ASTM International. Standard practice for assessment of hemolytic properties of materials. ASTM F756-08. West Conshohocken (PA): ASTM International; 2008.
42. Qin Z, Babu VS, Li Y, Shi F, Zhan F, Liu C, *et al*. Hemoglobin mediates inflammation and apoptosis in the head-kidney macrophages of grass carp (Ctenopharyngodon idella). Aquaculture. 2022;557:738281.
43. Riedmann K, Meegan J, Cervantes-Cruz Y, Ware L, Bastarache J. Cell-free hemoglobin induces vascular and mitochondrial dysfunction in the pulmonary endothelium in an oxidation-state dependent manner. Physiology. 2024;39(S1):1869.
44. Sabino RM, Kauk K, Movafaghi S, Kota A, Popat KC. Interaction of blood plasma proteins with superhemophobic titania nanotube surfaces. Nanomedicine. 2019;21:102046.
45. Sabino RM, Popat KC. Evaluating whole blood clotting *in vitro* on biomaterial surfaces. Bio Protoc. 2020;10 (3):e3505-e.